Journal of Magnetic Resonance **147,** 371–377 (2000)
doi:10.1006/jmre.2000.2212, available online at http://www.idealibrary.com on IDEAL®

# An Integrated Confocal and Magnetic Resonance Microscope for Cellular Research

Robert A. Wind,*[,1] Kevin R. Minard,* Gary R. Holtom,* Paul D. Majors,* Eric J. Ackerman,* Steven D. Colson,* David G. Cory,† Don S. Daly,* Paul D. Ellis,* Noelle F. Metting,* Chris I. Parkinson,* John M. Price,* and Xiao-Wu Tang†

**Pacific Northwest National Laboratory, P.O. Box 999, Richland, Washington 99352; and*
*†Department of Nuclear Engineering, MIT, Cambridge, Massachusetts 02139*

Received May 12, 2000; revised August 16, 2000

**Complementary data acquired with different microscopy techniques provide a basis for establishing a more comprehensive understanding of health and disease at a cellular level, particularly when data acquired with different methodologies can be correlated in both time and space. In this Communication, a brief description of a novel instrument capable of simultaneously performing confocal optical and magnetic resonance microscopy is presented, and the first combined images of live *Xenopus laevis* oocytes are shown. Also, the potential benefits of combined microscopy are discussed, and it is shown that the *a priori* knowledge of the high-resolution optical images can be used to enhance the boundary resolution and contrast of the MR images.** 

*Key Words:* **magnetic resonance microscopy; confocal scanning fluorescent microscopy; integrated microscopy; cellular research; *Xenopus laevis* oocytes.**

---

It is well recognized that magnetic resonance microscopy (MRM) and confocal optical microscopy (OM) each has their unique advantages and disadvantages when applied to studies of live cells (*1–3*). For example, while optical images can be acquired with a high spatial and temporal resolution, the application of OM is largely limited to transparent and stained samples. Conversely, while MRM is well suited to optically opaque samples and generally requires no exogenous contrast agents, the method is sensitivity limited. In practice, this means that both the temporal and the spatial resolution achieved with MRM is generally considerably less than that achieved with OM. Despite these shortcomings, however, MRM is extremely useful as it can provide both biophysical and biochemical information that cannot be obtained with OM and that is particularly useful for understanding health and disease at a cellular level (*4–16*). Therefore, correlating the OM and MRM data provides significant advantages over each of the methodologies individually.

In principle this approach can be realized by carrying the cells from one type of microscope to another (*17*). This approach has the advantage that it is relatively easy to implement and is especially well suited to studying fixed immobilized cells. However, when working with live cells a major disadvantage is that any change in the cell position, structure, and chemical composition that occurs between successive measurements inevitably jeopardizes an accurate correlation of acquired data. Moreover, imaging with different microscopes precludes studies of dynamic events where repetitive measurements are a prerequisite. These problems are avoided in a combined microscope where the same sample can be studied simultaneously with different methodologies. This Communication describes initial results for an integrated confocal and magnetic resonance microscope which is designed to study large single biological cells and cell agglomerates up to 0.8 mm in diameter.

The combined OM/MR microscope employs a modular architecture that separates optical and NMR components. A detailed description of the instrument will be published separately; here only a brief overview will be given. Figure 1 shows a sketch of the combined OM/MRM microscope. It utilizes an 89-mm diameter, vertical-bore Oxford magnet, operating at 11.7 T, into which a bottom-loading OM probe and a top-loading MRM probe are inserted. Proton magnetic resonance images are acquired using a Varian, Unity-Plus imaging spectrometer. The MRM probe consists of two parts: an outer probe containing the gradient coils, and an inner probe containing the RF circuit and the sample compartment. The sample compartment housing is machined from Torlon and has a glass window in the bottom. It contains the NMR coil wound onto a horizontally aligned silica capillary sample tube (1-mm OD, 0.8-mm ID, 6-mm length) and the remaining volume is filled with deionized deuterium oxide ($D_2O$) to improve both the optical and the magnetic properties of the test section. The sample tube is part of a perfusion system, which is used to transport the cells to the test section and to maintain their viability. In order to locate the cells in the center of the coil a polystyrene rod with a 0.25-mm diameter is mounted perma-

[1] To whom correspondence should be addressed at Pacific Northwest National Laboratory, P.O. Box 999, MS K8-98, Richland, WA 99352. Fax: (509) 376-2303. E-mail: robert.wind@pnl.gov.



1090-7807/00 $35.00

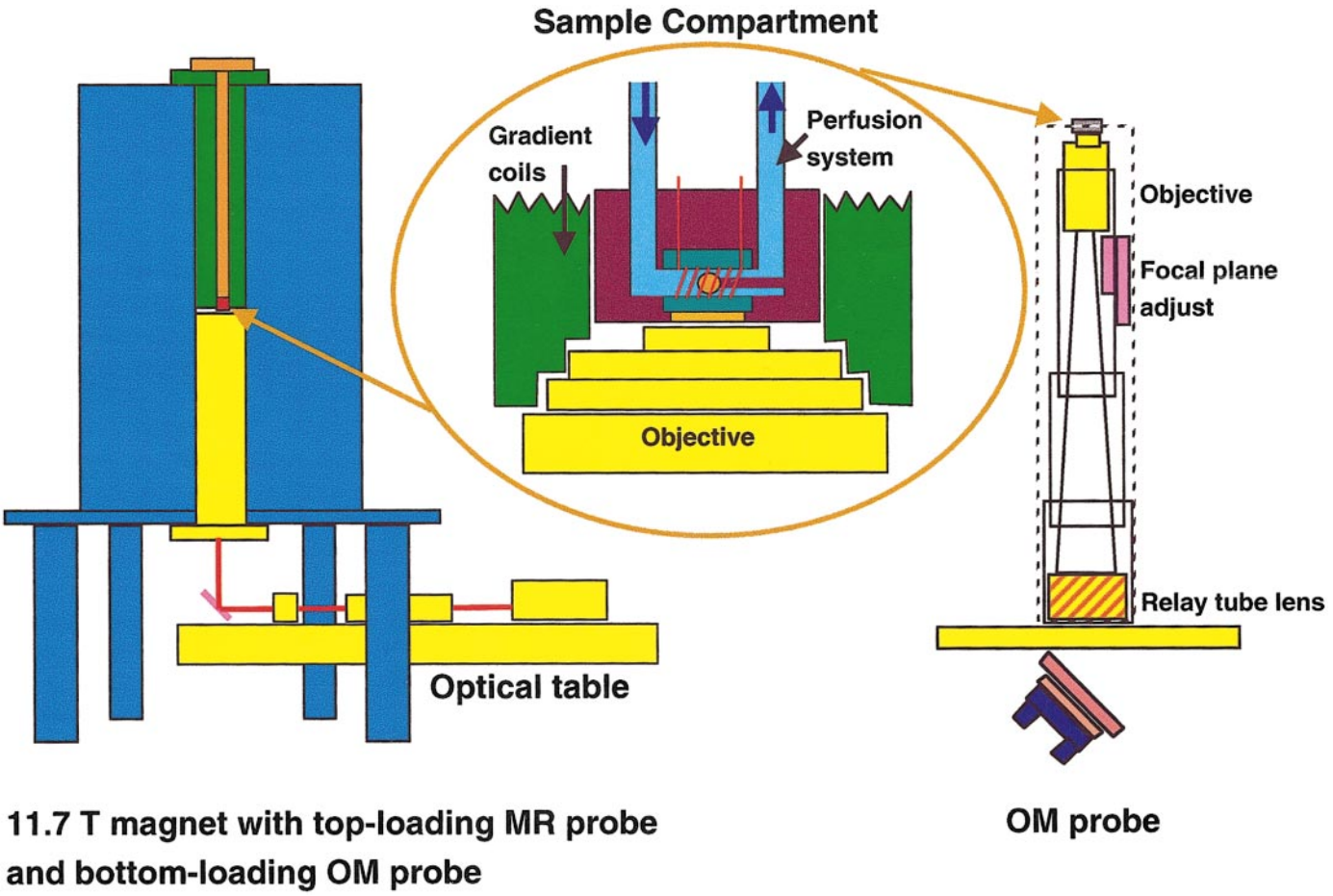


**FIG. 1.** Combined microscope architecture.

nently in the capillary at the outlet end, which is adequate to stop larger cells with a diameter of 0.4 mm and above. Smaller cells are retained by inserting a 0.53-mm-diameter solid polystyrene bead as an extra obstruction, injected into the capillary prior to inserting cells. The NMR coil is a solenoid with a length of 2 mm, consisting of eight turns of copper wire with a thickness of 30 $\mu$m and a wire spacing of 220 $\mu$m between the wires. This thin wire is used to minimize distortions in the optical images due to the presence of the coil. The $D_2O$ surrounding the coil has a magnetic susceptibility close to that of copper and serves to reduce the susceptibility broadening of the NMR lines due to the copper wires. It was found that the $D_2O$ does not induce any observable decrease in NMR performance of the coil at the 500-MHz proton Larmor frequency. With this setup a linewidth of about 0.003 ppm was observed in a water volume of $0.2 \times 0.2 \times 0.2$ mm$^3$ selected in the center of the coil, which is more than adequate for cellular research, where the linewidths are typically at least an order of magnitude larger (*16*).

The confocal scanning microscope consists of the bottom-loading probe with a custom objective manufactured from nonmagnetic materials by Special Optics. Additional design requirements were a field of view $2 \times 2$ mm$^2$ and a long working distance design as dictated by the gradient coil geometry. The objective contains 10 elements and has the highest practical numerical aperture of 0.45. Following the objective is a series of relay and scan lenses that place the galvanometer scanners 2 m away from the sample region. The objective can be moved in the vertical direction for three-dimensional imaging. A small 488-nm laser, with a fiber optic link, and a confocal detection system were placed about 3 m from the magnet to avoid interference. An isotropic resolution in the *xy*-plane up to 1 $\mu$m could be achieved, whereas the point-spread function in the *z*-direction perpendicular to the plane has a half-intensity width of about 33 $\mu$m. We compared the point-spread functions of our microscope with that of a commercial confocal microscope (Sarastro, manufactured by Molecular Devices), with the same numerical aperture. It was found that in our microscope the resolution in the *xy*-plane is about 85%, and the resolution in the *z*-direction is about 50% of that obtained with the Sarastro microscope. The reasons for this reduced image quality are under investigation and probably are a result of the fact that our confocal microscope is a more complex system than usual. The NMR coil wires are

partly present in the optical window, causing intensity variations in the optical field of view. These intensity distortions have been removed by normalizing the intensity of each image pixel with confocal imaging data acquired with the sample chamber uniformly filled with a fluorescent dye.

Initial testing of the combined microscope was performed using *Xenopus laevis* oocytes. These amphibian cells are intensively studied with light and confocal microscopy (*3, 18, 19*) because of their unique biology and relevance to human cells (*20*). In the current study, they were ideal for testing because their enormous sizes (0.2–1.3 mm) enabled detailed imaging—even with MRM (*21–25*). Moreover, they do not require an extremely high spatial resolution in the optical images, so that air objectives with a long working distance and a large field of view can be used.

Confocal fluorescence images and MR water and lipid images were obtained on oocytes of different growth stages. Prior to the image experiments, the oocytes and their surrounding follicle particles were stained with rhodamine-123, a nontoxic fluorescent dye selective for active mitochondria. Then the stained oocytes were injected into the perfusion system filled with Barth's medium, and the flowing medium transported the oocytes into the sample chamber and pressed them against the constriction in the perfusion tube, c.f. Fig. 1. This process was monitored in real time with a video camera and white-light, front-face illumination microscopy utilizing the same objective as that used for the confocal imaging. When the cells were positioned in the field of view, the flow was stopped in order to avoid flow artifacts in the MR images. Then a confocal 3D image was obtained, followed by MR 3D imaging and concluded by another confocal image to ensure that the cells did not move during the experiments. Hence the OM and MRM experiments were not rigorously performed simultaneously (this does not mean, however, that the experiments could have been performed with separate microscopes, because moving the sample chamber from one microscope to the other would cause major dislocations in the cell positions).

In order to register and calibrate the OM and MRM image spaces a 0.53-mm translucent polystyrene bead was injected prior to the insertion of the oocyte cells. This bead is easily imaged with MRM as a dark sphere in the surrounding medium, and also with OM, as the medium produced a weakly fluorescent signal resulting from a small fraction of the dye leaking from the oocytes into the medium. Moreover, the OM and MRM images of the medium also revealed the position of the tube walls. It was found that the information about the bead and tube locations was sufficient to obtain registration within the optical and MR image planes with accuracy mainly dictated by the MR voxel size. The registration in the direction perpendicular to the optical plane is less accurate as a result of the relatively large optical point-spread function in this direction. It is estimated that the accuracy in the image registration in this direction is about 40 $\mu$m. Currently phantom samples are under development to better characterize and improve this situation.

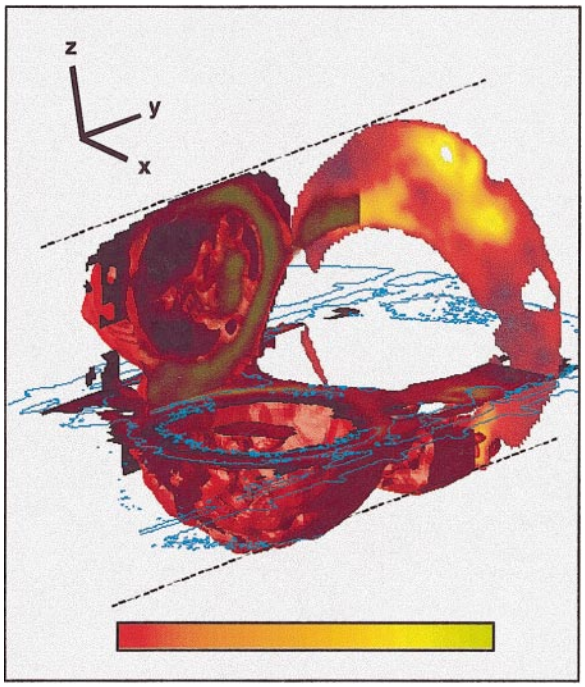


**FIG. 2.** Three-dimensional rendering of the MR image of a sample consisting of two stage 3 *Xenopus laevis* oocytes, a polystyrene bead, and some connective tissue and smaller oocytes. Experimental details are given in the legend to Fig. 3. The scale bars in the *x*-, *y*-, and *z*-directions are 0.2 mm in length. The blue contour plot shows the OM image plane coinciding with the horizontal MR plane, both shown in Fig. 3. The dotted lines represent the inner boundary of the 0.8-mm-ID sample tube. The MR rendering was zero-filled to yield an apparent 10-$\mu$m isotropic resolution.

Figure 2 shows a 3D rendering of the MR water image, obtained with the combined microscope. Two stage 3 oocytes with diameters of 0.6–0.7 mm are observed, connected to each other. The transparent object is the top half of the bead, and some smaller oocytes and connective tissue are located near the bottom of the sample tube. Also shown is the MR image of a horizontal plane near the diameter of the lowest stage 3 oocyte (with an average diameter of 0.62 mm) and the bead, and the contour plot of the OM image. In Fig. 3 the 2D OM and MRM images of the same plane are shown. With MRM, the distribution of both water and mobile lipids were imaged. In the OM image the right side of the bead and the top right side of the oocyte are poorly defined. This is due to the presence of three small oocytes in the optical path and below the OM plane, which produce shadows in the plane of interest. The high OM intensity at the oocyte boundary is believed to arise from the mitochondria in the surrounding follicle cell layer, while the interior is optically opaque. Additional features include stained connective tissue near the oocyte, a fluorescing layer along the inner wall of the sample tube, and a slight horizontal banding due to imperfect wire correction. As discussed previously, the quality of the optical image is less than optimal, resulting in some blurring of the sharp features.

The corresponding water MR image (Fig. 3b) is not affected

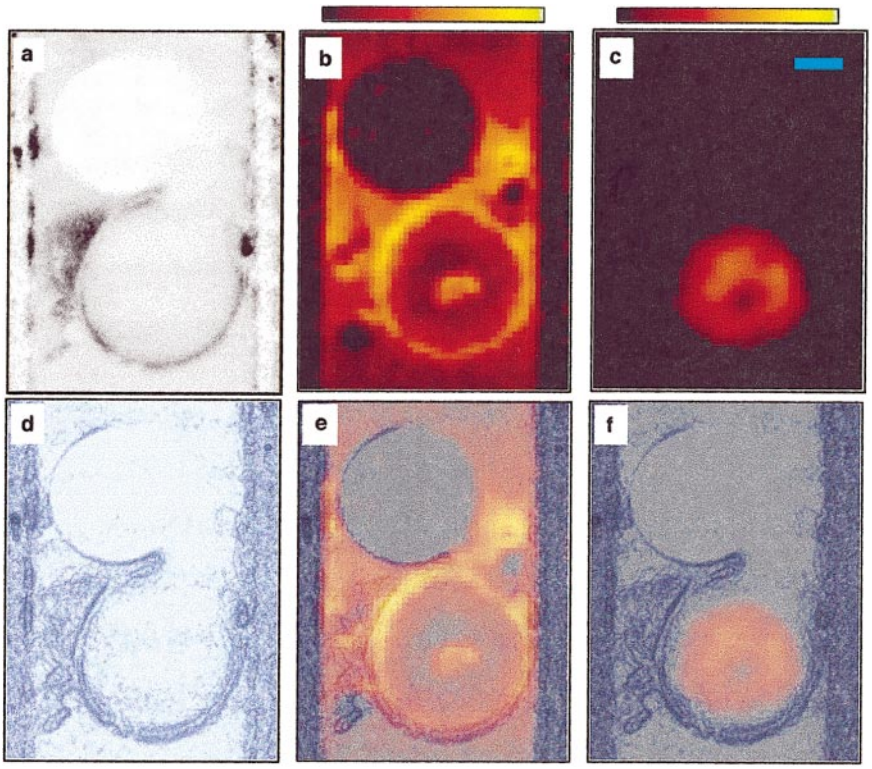


**FIG. 3.** Two-dimensional combined confocal optical (OM) and magnetic resonance (MR) images of a 0.53-mm-diameter polystyrene bead (top object) and a 0.62-mm-diameter stage 3 *Xenopus laevis* oocyte (bottom object) in an 0.8-mm-ID glass capillary tube. The oocyte was stained with the rhodamine-123 mitochondrial dye. The images represent the same horizontal plane through the center of the bead: (a) an OM image, corrected for intensity variations due to partial optical obstruction by the NMR coil wires; (b) a water-selective MR image; (c) a lipid-selective MR image; (d) an OM relief contour image, obtained from image (a); (e) an overlay of the water MR image with the OM relief image; and (f) an overlay of the lipid MR image with the OM relief image. The confocal image plane was collected as part of a 25-plane 3D stack. The in-plane optical image resolution is $3.9 \times 3.9\ \mu m^2$, the plane thickness is about 33 $\mu$m, and the entire stack was collected in about 5 min. An identical OM stack (not shown) of the sample chamber filled with fluorescent dye was collected and used to correct for intensity distortions in the optical images due to the presence of the coil wires in the optical field of view. Water and lipid MR images were obtained using a 3D FT spin warp MRI sequence using a repetition time of 0.5 and 0.3 s, respectively, and an echo time of 12 and 10 ms, respectively. Sixty-four phase-encoding steps were performed independently in each of the two directions mutually orthogonal to the tube axis, and 128 frequency-encoding points were sampled in the tube axis direction (frequency resolution is 200 Hz), yielding an isotropic spatial resolution of 20 $\mu$m. No zero filling was applied to the images in this figure. Water and lipid MR images were collected in 140 min with 4 repetitions and 210 min with 10 repetitions, respectively. A spectrally selective RF excitation pulse (2-kHz bandwidth) was employed to obtain chemically selective images. The scale bar shown in (c) is 0.2 mm in length.

by optical transmission effects and clearly shows the entire bead boundary. Also, the image shows a water-intensive nucleus and a layer of enhanced water intensity in the cytoplasm near the outer membrane. This enhanced intensity is mainly due to the fact that this water has a relatively short $T_1$ value and that a short repetition time was used in the experiment. The cytoplasmic water distribution is complemented by the lipid distribution in image (Fig. 3c), i.e., the water concentration is lower where the lipid distribution is higher and vice versa. The dark circles, observed in the water image on either side of the oocyte, are small air bubbles.

The OM/MR overlay images (Figs. 3e and 3f) combine the superior spatial resolution of OM with the rich chemical information and insensitivity to optical effects of MR. This simple integration of the techniques illustrates how OM can be used to enhance MR resolution, and MRM can complement OM data in opaque areas. Further, combined images can be used to identify features observed with the other imaging modality. Finally, Figs. 3e and 3f show that within the uncertainties imposed by the spatial resolution, contrast, and the signal-to-noise ratio of acquired images, excellent spatial registration is observed.

Figure 4 shows similar confocal and MR images obtained on a smaller stage 2 (0.38-mm-diameter) transparent oocyte. In contrast to results obtained on the larger oocyte (Fig. 3), the confocal image clearly shows the mitochondrial cloud (Figs. 4a and 4d). In the water MR image (Fig. 4b) only the inside layer of enhanced water intensity is detected. The mitochondrial cloud is not prominent in this image, although in other MR images of similar-size oocytes (not shown) a compartment of a similar dimension as the mitochondrial cloud and increased water intensity was visible. Further investigations are continuing to see whether indeed these compartments are mitochondrial clouds and under which conditions they become visible

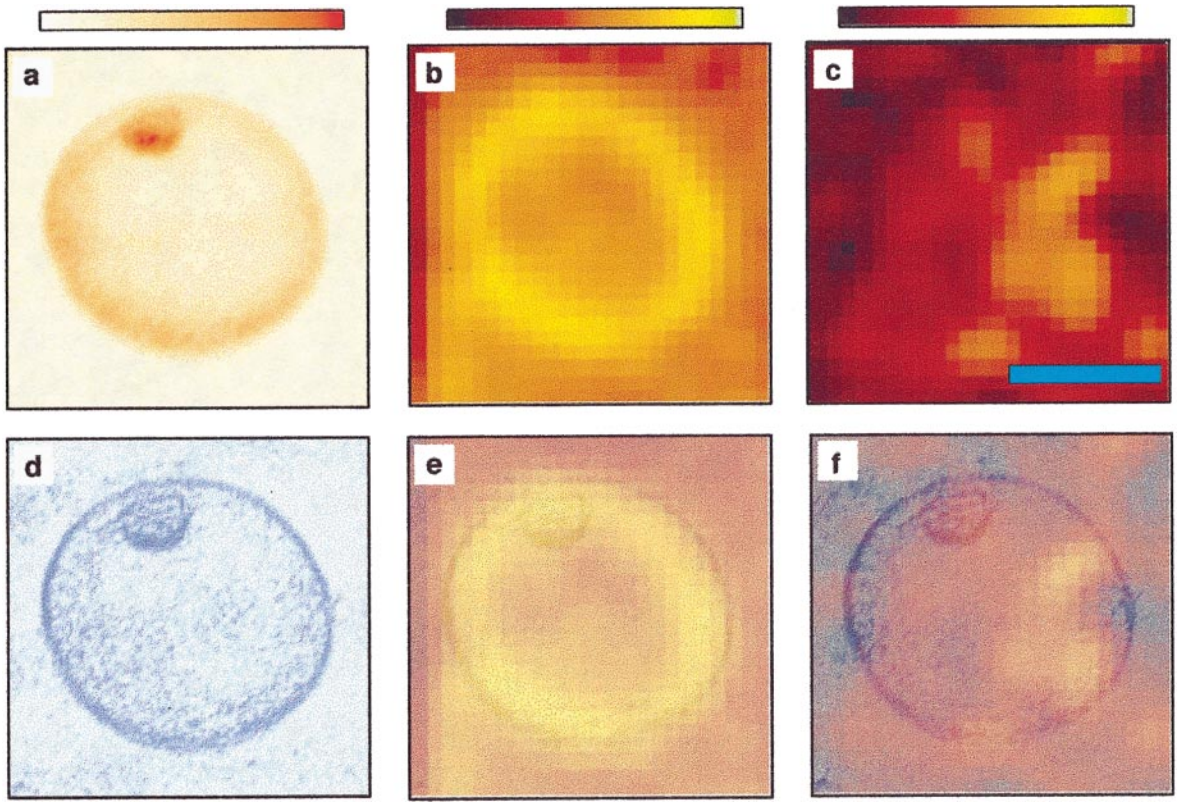


**FIG. 4.** Combined confocal optical (OM) and magnetic resonance (MR) images of a 0.38-mm-diameter stage 2 *Xenopus laevis* oocyte stained with rhodamine-123 mitochondrial dye. The images represent the same horizontal plane through the center of the oocyte: (a) an OM image, corrected for intensity variations due to partial optical obstruction by the NMR coil wires; (b) a water-selective MR image; (c) a lipid-selective MR image; (d) an OM relief contour image, obtained from image (a); (e) an overlay of the water MR image with the OM relief image; and (f) an overlay of the lipid MR image with the OM relief image. The image conditions are the same as given in the legend to Fig. 3, except that the in-plane resolution of the confocal image was enhanced to $2 \times 2\ \mu m^2$. The scale bar shown in (c) is 0.2 mm in length. No zero filling was applied to the images in this figure.

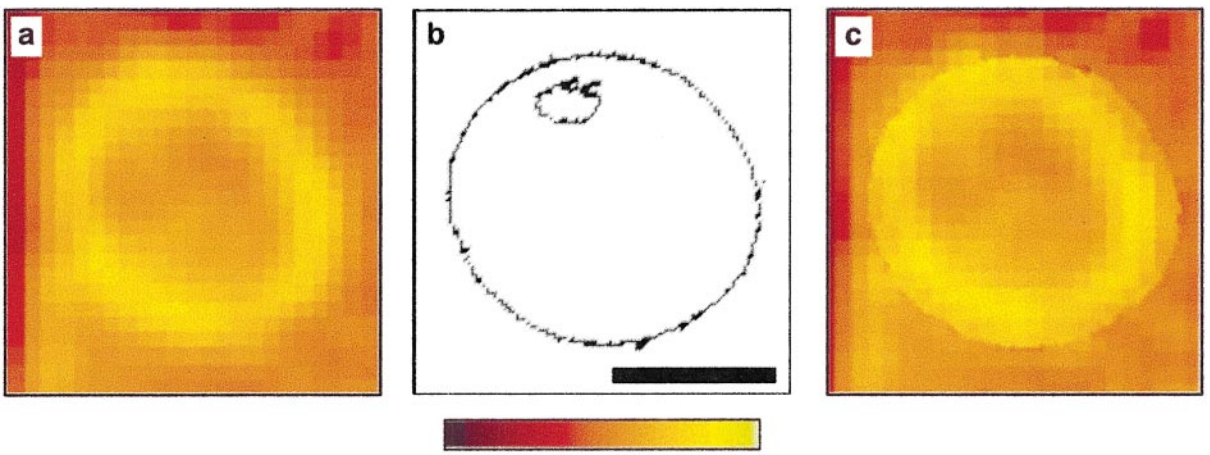


**FIG. 5.** Application of confocal image data to enhance the resolution and contrast of MR images at object boundaries. (a) The same MR water image of the stage 2 oocyte as shown in Fig. 4b; (b) a contour plot, obtained from the optical image shown in Fig. 4a; (c) an MR image with enhanced resolution and contrast near the contour boundaries. Enhancement was achieved by overlaying images (a) and (b) to distinguish MR image pixels containing the boundaries between the cell and the surrounding medium. Next, these MR boundary pixels were segmented by the confocal boundaries and assigned new intensities. The intensity calculations preserve the total intensity of the original pixel, employ the areas of the compartments in a pixel as determined by OM, and use the intensities in adjacent pixels completely embedded within a certain compartment. The scale bar shown in (b) is 0.2 mm in length. No zero filling was applied to the images in this figure.

with MRM. As expected for previtellogenic oocytes, only a very weak lipid image was observed, with an intensity that is at least a factor of 20 lower than the lipid signal observed in the larger stage 3 oocytes.

The results clearly illustrate that combined microscopy provides significantly more information than obtained with each of the techniques individually. The MR images provide detailed information about the intracellular structure of the larger opaque oocyte that is not observed with OM. On the other hand, in the smaller transparent oocytes, the high-resolution optical images can be used to complement the relatively low-resolution MR images. Moreover, the *a priori* knowledge provided by the confocal image can be used to improve the boundary resolution and the contrast in the MR images. This is illustrated in Fig. 5. Figure 5a shows the same MR water image of the stage 2 oocyte as that given in Fig. 4b, and in Fig. 5b a contour plot is given of the optical image shown in Fig. 4a. By overlaying both images pixels can be identified in the MR image containing the boundary between the oocyte and the surrounding medium. Then the average intensity in each of these pixels can be redistributed into each compartment inside these pixels, following the procedure described in the caption of Fig. 5. Figure 5c shows the resulting MR image. It follows that both the boundary resolution and the contrast are significantly enhanced. Hence integrated OM/MRM can be used to produce images in which the optical spatial resolution is combined with the MR contrast (and it is expected that this contrast can be further improved, e.g., by doping the cells with a proper contrast agent (*26, 27*)). In spirit, this is similar to the approaches currently used for improving low-resolution near-infrared optical images using the higher resolution MR images (*28*).

In summary, we have demonstrated that integrated OM/MR microscopy can significantly enhance the utility of both techniques. It is anticipated that a complete integration of optical and MR microscopy could result in a variety of new technical developments. For example, boundaries of organelles in large cells or specific areas in cell agglomerates observed in optical images could, in principle, be used to guide volume-selective MRM experiments (*29*) to obtain MR spectra of identified regions. Moreover, time-dependent cellular phenomena readily observed with optical microscopy could, in principle, be used to synchronize quantitative MR studies to a physiological activity. This is especially important for events that oscillate on a short time scale compared to the MRM measuring time—such as the release of insulin triggered by glucose (ca. 3/min) in pancreatic beta cells (*30*). In future applications, the instrument described here will be exploited for studying dynamic processes such as transport and stress responses in oocytes. Also, a second integrated microscope capable of examining single layers of live mammalian cells is under development. This will be used to study cell apoptosis, a process of critical importance to cancer therapy. It is anticipated that both instruments will, ultimately, greatly enhance the speed, specificity, and utility of OM and MRM methods in biomedical research. Therefore, combined OM–MRM may become one of the next generation microscopy instruments for cellular research.

## ACKNOWLEDGMENTS

The research was performed in the Environmental Molecular Sciences Laboratory, a national scientific user facility sponsored by the Department of Energy's Office of Biological and Environmental Research and located at Pacific Northwest National Laboratory.

## REFERENCES

1. P. Blümler, B. Blümich, R. E. Botto, and E. Fukushima, Eds., "Spatially Resolved Magnetic Resonance," Wiley-VCH, Weinheim (1998).
2. N. R. Aiken, E. W. Hsu, and S. J. Blackband, A review of NMR microimaging studies of single cells, *J. Magn. Reson. Anal.* **1,** 41–48 (1995).
3. J. B. Pawley, Ed., "Handbook of Biological Confocal Microscopy," Plenum, New York (1995).
4. P. F. Daly and J. S. Cohen, Magnetic resonance spectroscopy of tumors and potential in vivo clinical applications: A review, *Cancer Res.* **49,** 770–779 (1989).
5. M. Neeman, H. Eldar, E. Rushkin, and H. Degani, Chemotherapy-induced changes in the energetics of human breast cancer cells; $^{31}$P- and $^{13}$C-NMR studies, *Biochim. Biophys. Acta* **1052,** 255–263 (1990).
6. B. D. Ross, The biochemistry of living tissues: Examination by MRS, *NMR Biomed.* **5,** 215–219 (1992).
7. W. Negendank, Studies of human tumors by MRS: A review, *NMR Biomed.* **5,** 303–324 (1992).
8. C. E. Mountford, G. Grossman, G. Reid, and R. M. Fox, Characterization of transformed cells and tumors by proton nuclear magnetic resonance spectroscopy, *Cancer Res.* **42,** 2270–2276 (1982).
9. L. C. Wright, G. L. May, M. Dyne, and C. E. Mountford, A proteolipid in cancer cells is the origin of their high-resolution NMR spectrum, *Fed. Eur. Biochem. Soc. Lett.* **203,** 164–168 (1986).
10. G. L. May, L. C. Wright, K. T. Holmes, P. C. Williams, I. C. P. Smith, P. E. Wright, R. M. Fox, and C. E. Mountford, Assignment of methylene proton resonances in NMR spectra of embryonic and transformed cells to plasma membrane triglyceride, *J. Biol. Chem.* **261,** 3048–3053 (1986).
11. M. Stubbs, R. C. Coombes, J. R. Griffiths, R. J. Maxwell, L. M. Rodrigues, and B. A. Gusterson, $^{31}$P-NMR spectroscopy and histological studies of the response of rat mammary tumours to endocrine therapy, *Br. J. Cancer* **61,** 258–262 (1990).
12. S. M. Cohen and L. B. Ellwein, Cell proliferation in carcinogenesis, *Science* **249,** 1007–1011 (1990).
13. A. C. Kuesel, G. R. Sutherland, W. Halliday, and I. C. P. Smith, 1H MRS of high grade astrocytomas: Mobile lipid accumulation in necrotic tissue, *NMR Biomed.* **7,** 149–155 (1994).
14. F. G. Blankenberg, R. W. Storrs, L. Naumovski, T. Goralski, and D. Spielman, Detection of apoptotic cell death by proton nuclear magnetic resonance spectroscopy, *Blood* **87,** 1951–1956 (1996).
15. P. Weybright, K. Millis, N. Campbell, D. G. Cory, and S. Singer, Gradient, high-resolution, magic angle spinning $^{1}$H nuclear mag-

netic resonance spectroscopy of intact cells, *Magn. Reson. Med.* **39,** 337–345 (1998).

16. K. R. Minard, X. Guo, and R. A. Wind, Quantitative $^{1}$H MRI and MRS microscopy of individual V79 lung tumor spheroids, *J. Magn. Reson.* **133,** 368–373 (1998).
17. P. M. Glover, R. W. Bowtell, G. D. Brown, and P. Mansfield, A microscope slide probe for high resolution imaging at 11.7 Tesla, *Magn. Reson. Med.* **31,** 423–428 (1994).
18. M. V. Danilchik and J. C. Gerhart, Differentiation of the animal–vegetal axis in *Xenopus laevis* oocytes. I. Polarized intracellular translocation of platelets establishes the yolk gradient, *Dev. Biol.* **122,** 101–112 (1987).
19. D. L. Gard, Confocal microscopy and 3-D reconstruction of the cytoskeleton of *Xenopus* oocytes, *Micr. Res. Technol.* **44,** 388–414 (1999).
20. B. K. Kay and H. B. Peng, Eds., *Xenopus laevis:* Practical Uses in Cell and Molecular Biology, in "Methods in Cell Biology," Vol. 36, Academic Press, San Diego, 1991.
21. J. B. Aguayo, S. J. Blackband, J. Schoeniger, M. A. Mattingly, and M. Hintermann, Nuclear magnetic resonance imaging of a single cell, *Nature* **322,** 190–191 (1986).
22. S. Paüser, A. Zschunke, A. Khuen, and K. Keller, Estimation of water content and water mobility in the nucleus and cytoplasm of *Xenopus laevis* oocytes by NMR microscopy, *Magn. Reson. Imaging* **13,** 269–276 (1995).
23. Z. Gottesfeld and M. Neeman, Ferritin effect on the transverse relaxation of water: NMR microscopy at 9.4 T, *Magn. Reson. Med.* **35,** 514–520 (1996).
24. S. Posse and W. P. Aue, $^{1}$H spectroscopic imaging at high spatial resolution, *NMR Biomed.* **2,** 234–239 (1989).
25. R. E. Jacobs and S. E. Fraser, Magnetic resonance microscopy of embryonic cell lineages and movements, *Science* **263,** 681–684 (1994).
26. S. Paüser, A. Zschunke, and K. Keller, Interaction between paramagnetic metal complexes and intracellular water of single cells, *J. Magn. Reson. Imaging* **6,** 250–254 (1996).
27. A. Y. Louie, M. M. Huber, E. T. Ahrens, U. Rothbacher, R. Moats, R. E. Jacobs, S. E. Fraser, and T. J. Meade, In vivo visualization of gene expression using magnetic resonance imaging, *Nat. Biotechnol.* **18,** 321–325 (2000).
28. B. W. Pogue and K. D. Paulsen, High-resolution near-infrared tomographic imaging simulations of the rat cranium by use of a priori magnetic resonance imaging structural information, *Optics Lett.* **23,** 1716–1718 (1998).
29. R. Löffler, R. Sauter, H. Kolem, A. Haase, and M. von Kienlin, Localized spectroscopy from anatomically matched compartments: Improved sensitivity and localization for cardiac $^{31}$P MRS in humans, *J. Magn. Reson.* **134,** 287–299 (1998).
30. J. C. Henquin, J. C. Jonas, and P. Gilon, Functional significance of $Ca^{2+}$ oscillations in pancreatic beta cells, *Diabetes Metab.* **24,** 30–36 (1998).